17.1 Omnidirectional Magnetoelectric Power Transfer for Miniaturized Biomedical Implants via Active Echo

Wei Wang, Zhanghao Yu, Yiwei Zou, Joshua Woods, Prahalad Chari, Jacob T. Robinson, Kaiyuan Yang

Rice University, Houston, TX

Wireless, batteryless, and miniaturized implants promise transformative therapies for various neurological, psychiatric, and cardiac disorders. Beyond conventional battery-powered bulky implants with leads, miniaturized implants promise drastically reduced infection risk and surgical complexity, and improved patient acceptance and precision. Despite significant efforts on wireless power transfer (WPT) for implants, most demonstrations are not sufficiently reliable to sustain practical usage, when misalignment between the external hub and the implant persists due to motions, respiration, and heart beating, as well as the restricted device orientation during implantation (e.g. in spinal cords or vessels). The power transfer efficiency (PTE) of WPT degrade drastically under misalignment, rendering the system unstable and unusable (Fig. 17.1.1). Transmitting higher power is a simple way to power a misaligned implant but is restricted by safety limits, heating, and battery lifetime of the external device. It can be improved by introducing closed-loop regulation that adjusts the driver's power based on the implant's feedback [1,2]. However, this approach is only effective for smaller misalignment without addressing the fundamental efficiency drop. Recently proposed magnetoelectric (ME) WPT improves misalignment tolerance over existing inductive and ultrasound methods due to magnetic flux concentration effects [3]. Additionally, ME WPT at acoustic resonance (100s of kHz), is not subject to tissue absorption, reflection, and/or scattering issues met by RF, ultrasound, and optical WPT methods, allowing a miniaturized implant to receive high power at large depths reliably and safely [4]. However, ME WPT still cannot tolerate large rotations and lateral offset. On the other hand, multi-coil inductive WPT has made significant progress towards omnidirectional charging [5]. But existing multi-coil WPT are designed for high power applications (W to kW), with large TX/RX coils and high coupling coefficients (k>10%). Adopting these methods in miniature implants is nontrivial because the critical coupling sensing at the TX side cannot work with the tiny mutual inductance of mm-scale coils. Moreover, mutual inductance (M) among the TX coils degrades overall PTE. A 3D coil array cancels M effectively [6], but its spherical structure is bulky and incompatible with a wearable device for powering implants.

To tackle these challenges, this paper presents an Active Echo (AE) technique to achieve closed-loop omnidirectional WPT using a ME transducer weakly coupled to a multi-coil TX array (the equivalent coupling coefficient k <2% is estimated from TX-to-ME voltage transfer ratio). The key idea is to actively send a short echo signal from the implant, which allows the external hub to locate the implant and adjust power allocation within the multi-coil WPT array for magnetic field steering. By aligning the AE coil and ME transducer in the implant (physically perpendicular), we find that the ratio of coupling coefficients between AE and each coil in the external hub automatically equals the optimal current ratio of the multi-coil array for WPT, eliminating the need to explicitly obtain the implant's coordinate and calculate the multi-coil power allocation (Fig. 17.1.1). Moreover, the propagation of EM waves can be neglected in the quasi-static magnetic field assumption, so the multi-coil control only requires two polarities for the phase to approach the optimal point, simplifying the AE sensing and multi-coil control. To realize AE effectively and efficiently, we designed custom AE TX and RX chips in 180nm CMOS. We further demonstrate a complete system including a 14.2mm^3 ME powered and controlled bio-stimulation implant, a compact external hub including the custom AE RX, an M-canceled multi-coil array for both power transfer and AE sensing, and off-the-shelf GaN coil drivers and controller.

Figure 17.1.2 shows the block diagram of the external hub and the implant, and the implant's operation flow. When AE is activated, the implant turns on the pulse TX to drive a small LC tank for several cycles. Meanwhile, the external hub switches to AE sensing from WPT mode, and the echo signal is captured and processed to produce PWM control of the multi-coil in WPT. The mutual inductance (M) between the TX coils adds current-dependent imaginary parts to the impendence, degrading the power efficiency (Fig. 17.1.2 bottom right). In typical inductive coupling, slightly shifting the operating frequency compensates for the loss. However, the acoustically resonant ME transducer suffers greater energy loss when not operating at the exact resonant frequency. We observe that there should exist an optimal relative position for stacked coils, where the magnetic flux in the overlapping and non-overlapping regions cancels. HFSS simulation of a three-coil array confirms that stacked coils achieve a smaller M than parallel placement and avoid WPT dead zones at the boundary of coils. More importantly, decoupled coils allow simpler independent control of the coils.

Figure 17.1.3 presents the TX and RX circuits for Active Echo (AE). Based on the harmonic suppression principle [7], we designed the PA to produce a 3-level waveform, which results in a cleaner sine wave in the LC tank with lower high-order harmonics and less driving power. To suppress even-order harmonics, the inputs to the H-bridge PA must be non-overlapping with the same duty cycle and 180° phase shift. A self-biased fully differential VCO stage is designed to meet the requirements [8]. A programmable duty cycle adjustment block before PA shapes the signal. On the RX side, prior work on closed-loop ME WPT regulation [2] uses a separate pick-up coil for feedback from the implant, which works at a far-away frequency for lower interference. This approach is not suitable for our system because AE requires the pick-up coils to be perfectly aligned with the power coils and integrating them will complicate M cancellation and assembly of the multi-coil array. Here, since the TX driver's supply voltage is comparable to that of AE RX, we share the same coils for WPT and AE sensing in time division. With trade-offs among AE coil size, output power on the implant, self-resonant frequency of TX coil, and interference with the ~340kHz ME frequency, we designated AE to 1.35MHz. While WPT must be halted during AE sensing, the narrow AE window has negligible impact on the overall power transfer and operation of the implant. To capture the weak AE signal, we designed an inverter-based LNA with high gain and noise efficiency, followed by PGA and BPF. A peak detector and a single-slope ADC then extract the amplitude. Peak voltage sampling and comparator autozeroing are done simultaneously on a single cap. To extract the polarity (phase) of the signals, we first choose the strongest channel as the reference because in many scenarios one or two RX channels may not receive signals with sufficient SNR. Then we use digital logic to judge the polarity of received signals in other channels. Here, the channel with the fastest ADC conversion time is also the strongest one because of the reverse ramp signal. As a result, the polarity judgment only takes a few AE cycles.

We fabricated the two chips in 180nm CMOS and integrated them into a complete wireless system including a 3-coil TX array (Fig. 17.1.2). The 3-level PA produces symmetrical 3-level waveforms (Fig. 17.1.4 top left), achieving 30dB suppression of 3rd harmonic with 2.2dB fundamental tone reduction, and up to 27% power savings, over a baseline 2-level PA. The measured mutual inductance between two coils matches the simulation well, allowing us to find an optimal position with minimized coupling. The performance of the RX AFE and 7b ADC are measured (Fig. 17.1.4 middle), yielding an end-to-end rms noise of ~3 LSBs. This is sufficient for our 40-level PWM control of WPT drivers. The full system operation is shown in Fig. 17.1.4 (bottom), where the implant cycles through wireless charging, downlink programming, and four tasks (here task 1 is AE, task 3 is stimulation, and tasks 2 and 4 are skipped). The waveforms show biphasic stimulation at 100Hz and 50Hz, and the process of an AE task, including initialization, 16-cycle echo, and ringing down after stop.

We evaluated the closed-loop WPT performance of the complete system *in-vitro* through porcine tissue (Fig. 17.1.5). When the coupling coefficient of one channel is much smaller than another (the empirical threshold is 8), this channel will be turned off because PWM control has limited precision in these cases and the static power of a channel is more significant. We manually swept coil current configurations for Case 2 and 4, proving that AE obtains close-to-ideal current configurations with <2% PTE loss from the absolute optimum. In Case 4, when the implant is above TX3 and rotated by 30°, our system shows 66% higher PTE than using TX3 coil only. Fig. 17.1.6 presents PTE under angular and lateral misalignments, comparing our AE adaptive control, three coils with identical power and phase, and a single coil at the origin. AE consistently outperforms the others, especially under large misalignments. At 90° rotation from the perfect alignment, AE offers 6.8x higher PTE than the single-coil baseline, proving its omnidirectional WPT capability. Considering the voltage compliance of the logic-rule implant chip, we keep the total TX power under 0.5W, which is well below the driver power allowed by IEEE Std (i.e., 17.6W at 340kHz [2]). At 90° rotation, the implant still receives 4.45mW, sufficient for its operation. A comparison table with prior miniature biomedical implants is in Fig. 17.1.6. Die micrographs and summaries of the two chips are in Fig. 17.1.7.

Acknowledgement:
This work is supported by the National Science Foundation (NSF) CAREER program (2146476). The authors would like to thank Huan-Cheng Liao, Zhiyu Chen, Fatima T. Alrashdan, Yan He, and Xi Hu for technical discussions and support.

References:

[1] J. Tang, L. Zhao and C. Huang, "33.6 A Wireless Power Transfer System with Up-to-20% Light-Load Efficiency Enhancement and Instant Dynamic Response by Fully Integrated Wireless Hysteretic Control for Bioimplants," *ISSCC*, pp. 470-471, 2021.
[2] Z. Yu et al., "A Wireless Network of 8.8-mm^3 Bio-Implants Featuring Adaptive Magnetoelectric Power and Multi-Access Bidirectional Telemetry," *RFIC,* pp. 47-50, 2022.
[3] Z. Yu et al., "Magnetoelectric Bio-Implants Powered and Programmed by a Single Transmitter for Coordinated Multisite Stimulation," *JSSC*, vol. 57, no. 3, pp. 818-830, 2022.
[4] J. Chen et al., "A wireless millimetric magnetoelectric implant for the endovascular stimulation of peripheral nerves, " *Nat. Biomed. Eng*, 6, pp. 706–716, 2022.
[5] H. Qiu, T. Sakurai and M. Takamiya, "A 6.78-MHz Multiple-Transmitter Wireless Power Transfer System With Efficiency Maximization by Adaptive Magnetic Field Adder IC," *JSSC*, vol. 57, no. 8, pp. 2390-2403, 2022.

 979-8-3503-0620-0/24/$31.00

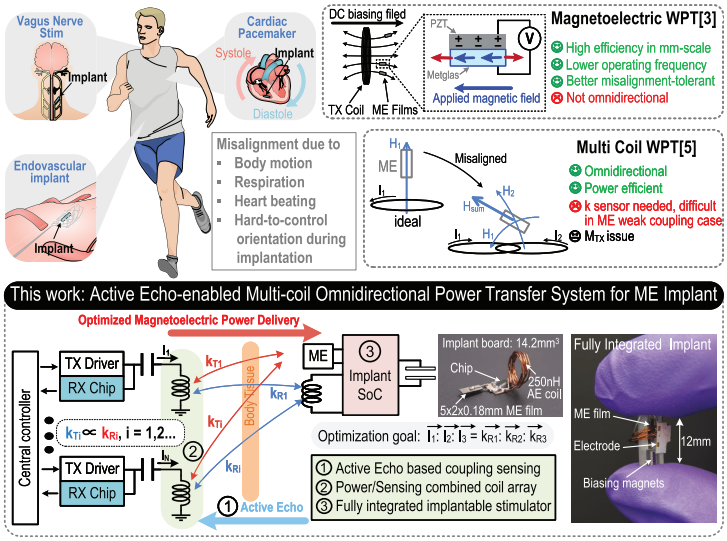

Figure 17.1.1: The misalignment challenge in wireless power transfer to mm-scale implants. Principles of the Active Echo-enabled omnidirectional magnetoelectric (ME) power transfer and a picture of the prototyping implant.

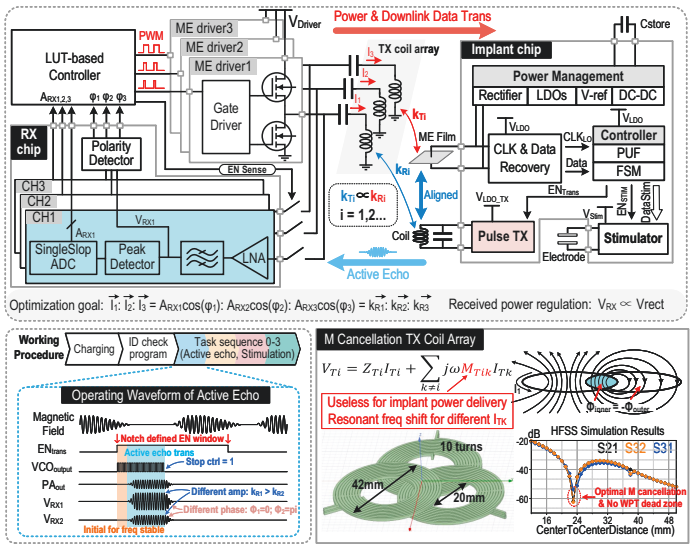

Figure 17.1.2: Diagrams of the system comprised of a mm-scale implant and a compact external hub; operation flow of the implant and Active Echo process; and mutual inductance cancellation in TX coil array.

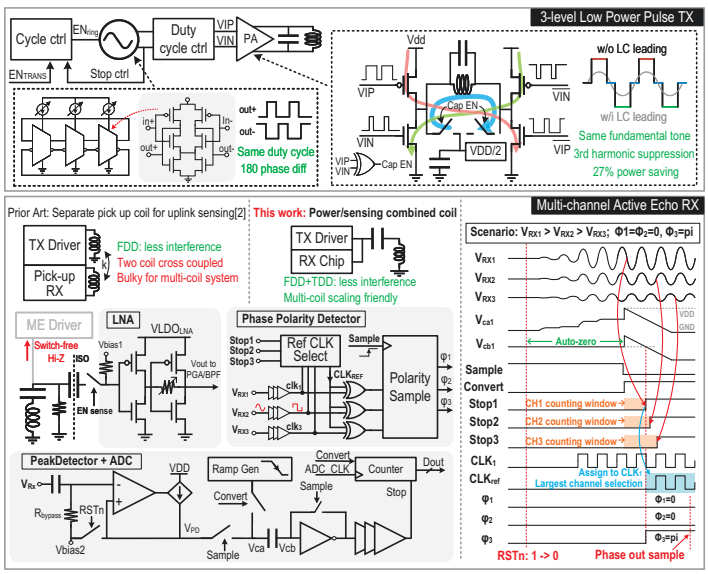

Figure 17.1.3: Circuit diagrams and operation waveforms of the 3-level low-power pulse TX and multi-channel Active Echo RX.

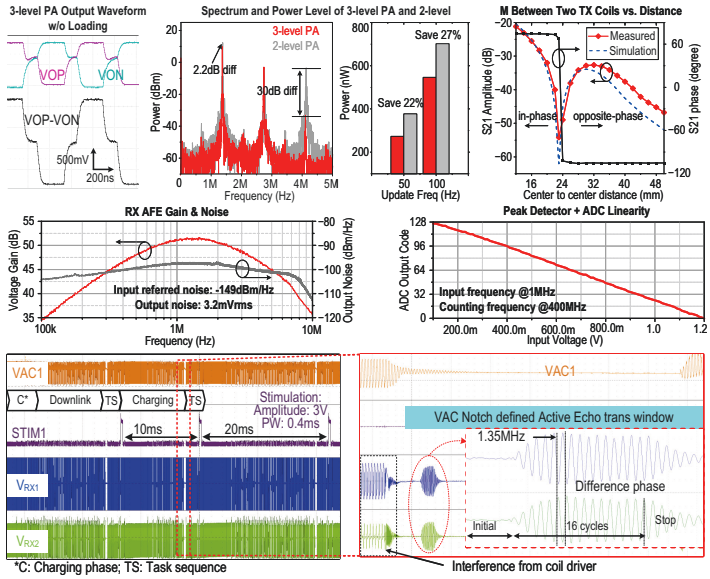

Figure 17.1.4: Measurement of 3-/2-level PA, TX coil array, and RX chain; and system operation waveforms when the implant is 90° rotated.

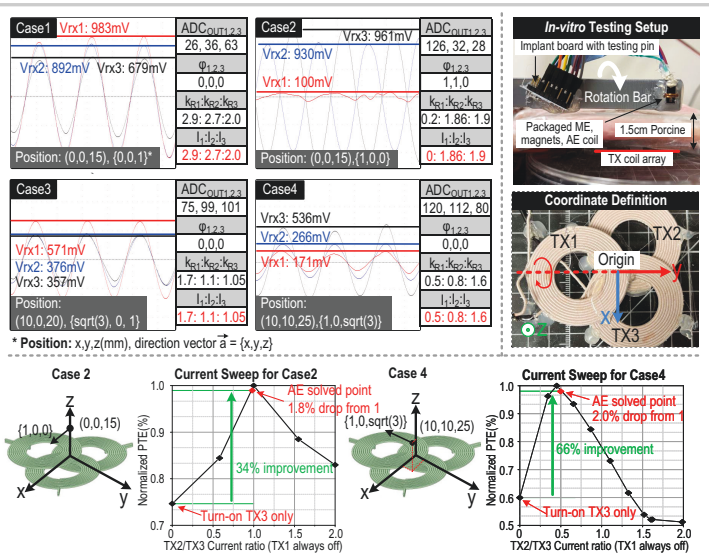

Figure 17.1.5: Measured 3-channel RX outputs (coupling coefficients, phases, and TX coil array configuration) at various positions; the *in-vitro* setup; and comparison of AE solved configurations and manual sweeps.

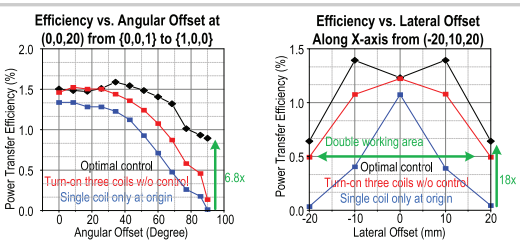

	This Work	Z. Yu RFIC'22 [2]	Z.Yu JSSC'22 [3]	J.Lee Nat. Elec.'21 [10]	J. Tang ISSCC'21 [1]	D. Piech Nat. BME'20 [9]
Technology(nm)	180	180	180	65	180	65
Bio-Application	Stimulation	Stimulation	Stimulation	Recording	N/A	Stimulation
WPT Mechanism	ME (340kHz)	ME (340kHz)	ME (330kHz)	Inductive (900MHz)	Inductive (6.78MHz)	Ultrasound (1.85MHz)
TX type	Planar Coil Array	Single Coil	Single Coil	TX Coil + Relay Coil	Single Coil	Single Transducer
Power Transducer Size (mm)	5×2×0.18	4×2×0.1	4×2×0.1	0.5x0.5 (on-chip)	25×25 (PCB)*	1×0.8×0.8
Global Regulation	Yes, Active Echo	Yes, LSK Backscatter	No	No	Yes, LSK Backscatter	No
Omnidirectional	Yes	No	No (< 50° rotation)	No	No	No (< 45° rotation)
Peak PTE (Aligned)**	1.58% (20mm)	0.2% (20mm)	0.5% (20mm)	0.08% (8mm)	61.9% (6.5mm)	0.06% (18mm)
Peak PTE (90° Rotation)**	0.89% (20mm)	N/A	0.045% (20mm)[$]	N/A	N/A	N/A
Maximum Received Power**	7.9mW (20mm)	N/A	N/A	0.025mW (8mm)	32mW (6.5mm)	0.0097mW (18mm)
FoM[#]	114	400	160	N/A	1000	5300

*Assume the thickness of PCB is 1mm; **TX-RX distance in (); [#]FoM = PowerTransducerVolume/PTE; [$]Read from figure

Figure 17.1.6: Measured PTE over angular and lateral misalignment; power breakdown of one RX channel; and a comparison table with state-of-the-art WPT technologies for biomedical implants.

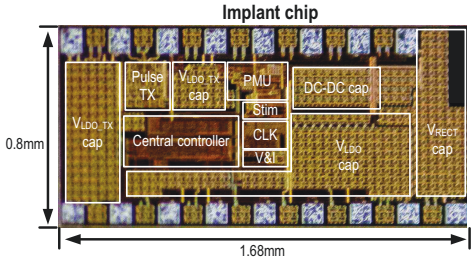

Stimulator Setting

Amplitude (4 bits)	1-3.5V
Pluse Width(3 bits)	0.05-1.5ms
Shape	Bi-phase, Monophasic
Frequency	0-200Hz Continuous change
Delay (4 bits)	0-1ms

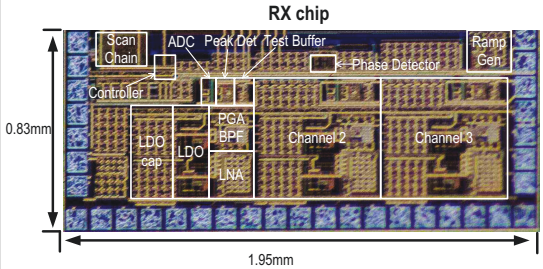

RX Single Channel Performance Summary

Technology	180
Power	Total: 18.65mW @400MHz
Area	0.147mm^2
Gain range	10-60dB with 1dB/Step
IRN	-149dBm/Hz
LPF BW	1M-8M
ADC bit	7

Figure 17.1.7: Chip micrographs of the implant's SoC and the RX chip, the stimulator's specifications, and a summary of RX performance.

Additional References:

[6] F. Huang et al., "30.8 3D Wireless Power Transfer with Noise Cancellation Technique for −62dB Noise Suppression and 90.1% Efficiency," *ISSCC*, pp. 452-453, 2023.
[7] J. Fritzin, C. Svensson and A. Alvandpour, "Design and Analysis of a Class-D Stage With Harmonic Suppression," *TCAS-I*, vol. 59, no. 6, pp. 1178-1186, 2012.
[8] A. Musa et al., "A Compact, Low-Power and Low-Jitter Dual-Loop Injection Locked PLL Using All-Digital PVT Calibration," *JSSC*, vol. 49, no. 1, pp. 50-60, 2014.
[9] D. K. Piech et al., "A wireless millimetre-scale implantable neural stimulator with ultrasonically powered bidirectional communication," *Nat. Biomed. Eng*, 4, pp. 207-222, 2020.
[10] J. Lee et al., "Neural recording and stimulation using wireless networks of microimplants," *Nat. Electron,* 4, pp. 604-614, 2021.

979-8-3503-0620-0/24/$31.00